JOURNAL OF PROPULSION AND POWER
Vol. 22, No. 5, September–October 2006

Numerical Simulation of a Real Shcramjet Flowfield

J. P. Sislian,* R. P. Martens,† and T. E. Schwartzentruber‡
University of Toronto Institute for Aerospace Studies, Downsview, Ontario, M3H 5T6, Canada
and
B. Parent§
Seoul National University, Seoul 151-744, Republic of Korea

DOI: 10.2514/1.14895

A shock-induced combustion ramjet (shcramjet) geometry is considered wherein the fuel, gaseous hydrogen, is injected in a two-oblique shock external compression inlet via cantilevered ramp injectors and a wall slot. The combustible mixture formed at the exit of the inlet is then ignited through the shock generated by the cowl of the engine. The numerical simulation of the three-dimensional flowfield of a shcramjet flying at $M = 11$ and at an altitude of 35 km was performed using the WARP code, in which multispecies Favre-averaged Navier–Stokes equations are closed by the k–ω turbulence model and the Wilcox dilational dissipation correction, to account for compressibility effects at high turbulence Mach numbers. The hydrogen/air chemical reactions are modeled by Jachimowsky's nine species, 20 reaction model. It has been found that the combustor length resulting from the shock-induced process is of the order of 25–30% of the inlet length. The relatively low value of the fuel specific impulse obtained, 573 s, is mainly due to incomplete mixing achieved in the adopted inlet model. To the authors' knowledge, the paper contains the first ever proof, in the open scientific literature, of the feasibility of this hypersonic propulsion concept in realistic flow situations, by numerical simulation.

Nomenclature

c	=	species mass fraction
E	=	total energy, $e + k + q^2/2$
e	=	internal energy
F	=	inviscid flux vector
$\boldsymbol{F}_{\text{skin friction}}$	=	force vector due to skin friction
G	=	vector of diffusion variables
h_k	=	enthalpy of species k
J	=	metric Jacobian
K	=	diffusion matrix
k	=	turbulence kinetic energy
M_c	=	convective Mach number, $(q_1 - q_2)/(a_1 + a_2)$
$\dot{m}_{\text{air,engine}}$	=	mass flow rate of air in the engine
n_s	=	number of species
P	=	pressure
P_0	=	freestream atmospheric pressure
Q	=	vector of conserved variables
q	=	magnitude of the velocity vector
R	=	residual
R_Δ	=	discretized residual
r	=	mesh dimensions factor
S	=	vector of source terms
T	=	temperature
T_0	=	freestream atmospheric temperature
V	=	contravariant velocity
v	=	velocity
$\dot{W}$	=	vector of species production terms (mass per unit time)
X	=	curvilinear coordinate
$X_{i,j}$	=	$\partial X_i/\partial x_j$
x	=	Cartesian coordinate
x, y, z	=	Cartesian coordinates
Y_n	=	normalized distance above lower duct wall
y^+	=	nondimensional wall distance, $\frac{\nu}{\mu}\sqrt{\rho\tau_w}$
ε	=	dissipation rate of the TKE
η_{m}	=	mixing efficiency
μ	=	viscosity
μ, κ, ν	=	viscosity, thermal conductivity and mass diffusion coefficient
ξ	=	convergence threshold
ρ	=	density
τ_w	=	wall shear stress
ϕ	=	global equivalence ratio
ω	=	turbulence dissipation rate

Subscript

b	=	station of interest

Superscripts

R	=	reacting
S	=	stoichiometric

Introduction

RECENT renewed research effort in shcramjets (*shock*-induced combustion *ramjets*) has generated some revealing results concerning, particularly, the propulsive characteristics of such engines. There is now some evidence that shcramjets can outperform the scramjets in the very high flight Mach number range. A detailed review of this early work is given in [1]. However, such conclusions were based on a number of very restrictive assumptions. For example, the shcramjet flowfield was assumed to be inviscid and the fuel injected in the forebody inlet of the engine to be homogeneously mixed before its ignition by a shock wave. Clearly, much more additional work is needed to definitely substantiate this claim. A number of problems have yet to be tackled if shcramjets are likely to be a technically feasible alternative to scramjets such as 1) the feasibility of quasihomogeneous fuel/air mixing in the high-temperature, high Mach number forebody airflow, avoiding premature ignition upstream of the combustion-inducing shock and in the forebody boundary layer; 2) realistic estimates of frictional

Received 2 December 2004; revision received 24 November 2005; accepted for publication 29 January 2006. Copyright © 2006 by Jean P. Sislian. Published by the American Institute of Aeronautics and Astronautics, Inc., with permission. Copies of this paper may be made for personal or internal use, on condition that the copier pay the $10.00 per-copy fee to the Copyright Clearance Center, Inc., 222 Rosewood Drive, Danvers, MA 01923; include the code $10.00 in correspondence with the CCC.

*Professor; sislian@caius.utias.utoronto.ca. Associate Fellow AIAA.
†Graduate Student; ryan.martens@utoronto.ca.
‡Graduate Student; tom.schwartzentruber@utoronto.ca.
§Research Associate, Department of Aerospace Engineering; bernard@snu.ac.kr.

forces and the effects of viscosity on the shock-induced combustion wave or detonation wave behavior in the narrow passage between the central body and the cowl of the engine; 3) the optimum choice between inlet shock intensities and that of the shock-induced combustion wave.

Lately, a comprehensive research effort has been made to address a few of the above mentioned tasks. In [2,3], an injector geometry is considered that is thought to be particularly suited for fuel/air mixing in shcramjet inlets. Dubbed cantilevered ramp injector, it embodies the characteristics of both wall-mounted ramp injectors [4] and low-angled wall injection [5]. The cantilevered ramp injector completely envelops and shields the fuel jet from the immediate high-temperature effects of impinging shock waves on the fuel jet, thus avoiding its premature ignition, and prevents the fuel from entering the hot boundary layer in the near field. Further, by injecting the fuel approximately in the same direction as the surrounding freestream direction, it ensures that the momentum of the fuel injected is recovered in the thrust balance. In these and subsequent papers [6,7], the results of a detailed and thorough analysis of the fuel/air mixing characteristics of such an injector were presented, with particular emphasis on the effects of the convective Mach number, global equivalence ratio, and geometrical parameters of the injector (injector array spacing, injection angle, and injector sidewall sweep angle). In all of these studies, the inflow properties of the oncoming air were kept constant and corresponded to flow conditions after the first shock of an external compression inlet of a shcramjet at a flight Mach number 11, where fuel injection is assumed to take place. At a flight dynamic pressure of 67 kPa, two equal-strength inlet shocks and 900 K temperature before the combustion-inducing shock, the resulting air properties after the first inlet shock were $p = 4758$ Pa, $T = 462$ K, and $M = 7.73$. Fuel jet conditions were varied depending on the convective Mach number and the global equivalence ratio considered. The two basic performance parameters employed to assess the fuel/air mixing characteristics resulting from the use of cantilevered ramp injectors were the air-based mixing efficiency and the concept of thrust potential [6]. Gaseous hydrogen was exclusively used as fuel.

The three-dimensional hypersonic, multispecies, turbulent flowfields resulting from the fuel/air mixing process in the above investigations were solved using the Favre-averaged Navier–Stokes equations closed by the Wilcox k–ω turbulence model [8] and the Wilcox dilational dissipation term [9] to account for compressibility effects occurring at high turbulent Mach numbers. Numerical results were obtained with the window allocatable resolver for propulsion (WARP) code developed at UTIAS. A detailed description of this computational technique is given in [10]. The marching window acceleration technique is used to obtain fast convergence to steady state. An extensive analysis of the predictive capabilities of the WARP code as applied to flow characteristics to hypersonic airbreathing propulsion is presented in [11].

The crucial task of fuel/air mixing in a high Mach number shcramjet inlet is tackled in [12]. The study is limited to nonreacting hydrogen/air mixing in a generic external compression inlet at a flight Mach number of 11, and a flight dynamic pressure of 67 kPa (1400 psf). Fuel is injected via a "near-optimal" array of cantilevered ramp injectors derived from earlier work [3,6,7] at a global equivalence ratio near unity and a convective Mach number of 1.2. The injector array is located between the first and second inlet compression processes, which are either shock waves or an oblique shock followed by a Prandtl–Meyer compression fan. The comparative mixing efficiency augmentation through an oblique and Prandtl–Meyer compression is analyzed in [13]. The main findings of the study of fuel injection in a shcramjet inlet of note are the following: the maximum air-based mixing efficiency obtained is 0.47 (i.e., only 47% of the available air in the inlet is mixed with the fuel); losses due to skin friction make up as much as 50–70% of the thrust potential losses; and cantilevered ramp injectors do succeed in keeping the fuel out of the hot boundary layer until the last 15% of the generic external compression inlet considered, where the second inlet shock compresses the mixture into the boundary layer. A chemically reacting study [14], involving nine species and 20 finite-rate reactions [15], of the mixing process considered, indeed revealed the occurrence of premature ignition primarily in the boundary layer, in the last 15% of the inlet, which spread into the core flow before the inlet exit. Both gaseous nitrogen and hydrogen were then injected through a wall slot into the inlet flowfield in an attempt at suppressing the flame. Premature ignition and subsequent flame propagation were suppressed in the entire flow by the slot injection of hydrogen just before the second inlet shock.

The concept of premixing the fuel in the inlet of a hypervelocity engine has lately gained interest with a view to improve the mixing and combustion efficiency of scramjets. A numerical investigation of fuel/air mixing in a Mach 8 inlet by means of an injector structurally detached from the engine and placed well upstream of the engine is reported in [16]. Livingston et al. [17], Owens et al. [18], and Gouskov et al. [19] considered normal injection of fuel behind thin pylons. Both the experimental [17] and numerical [18] results show that pylons contribute significantly to lift liquid or gaseous fuel from the surface, thus avoiding fuel in the boundary layer and potential flashback.

A numerical simulation of the three-dimensional flowfield of a real shcramjet and an assessment of its propulsive performance is described in the present paper. Gaseous hydrogen is injected in the inlet and the resulting combustible mixture ignited at the exit of the inlet, by the cowl-generated shock. To the authors' knowledge, the paper contains the first ever proof, in the open scientific literature, of the feasibility of this hypersonic propulsion concept in realistic flow situations by numerical simulation. The only other unsuccessful attempt at tackling a similar task within the framework of a two-dimensional turbulent reacting flowfield with one-equation turbulence model, at a flight Mach number of 12, is described in [20].

Shcramjet Model

A two equal-strength oblique shock external compression inlet is considered. Fuel (gaseous hydrogen) is injected via an array of optimized (for given flow conditions) cantilevered ramp injectors [6,12,14] located between the first and second inlet shocks. The cantilevered injectors used in the present study and their geometrical dimensions are shown in Fig. 1. The injector sidewalls have a negative sweep angle of -3.5 deg, and the injector spacing is set to 2 cm, twice the jet fuel width. The x position of the second inlet wedge is such that, when no fuel is injected, the two inlet shocks meet at $x = 1$ m, hence resulting in an inlet length $L_{\text{inlet}} = 1$ m. The overall inlet-injector configuration and relevant geometrical dimensions are given in Fig. 2.

The oncoming air flow conditions correspond to those of U.S. Standard Atmosphere at an altitude of 34.5 km at a flight Mach number of 11 and a flight dynamic pressure of 67,032 Pa (1400 psf). Therefore, the air pressure, temperature, density, and velocity entering the shcramjet inlet are $P_0 = 791$ Pa, $T_0 = 237$ K,

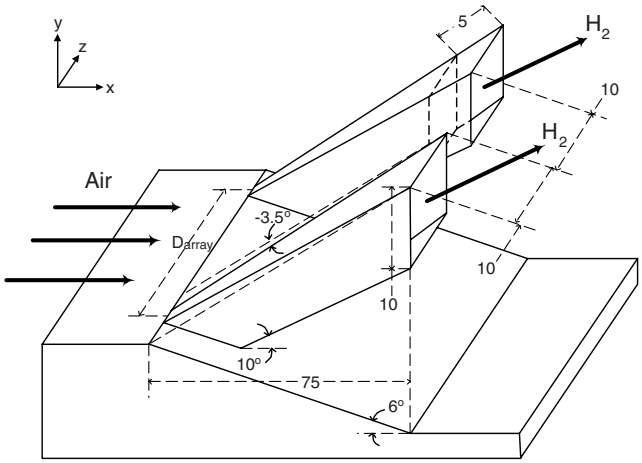

Fig. 1 Optimized cantilevered injector geometry (dimensions in mm) [12].

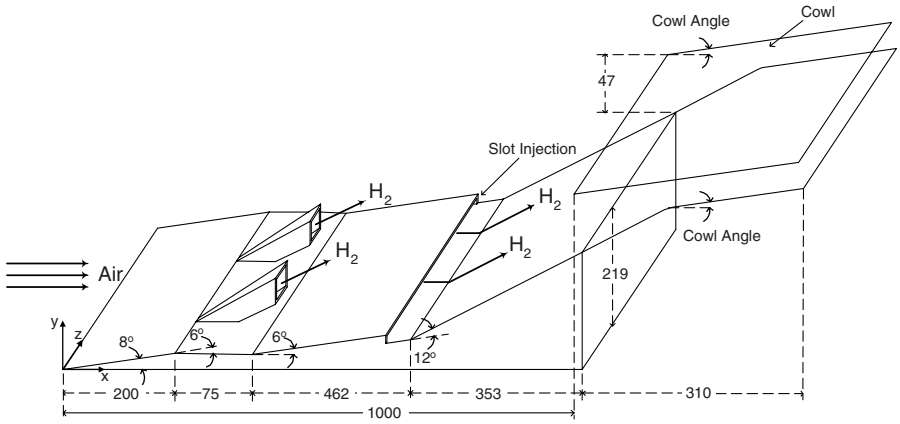

Fig. 2 Baseline dual spike shcramjet inlet and combustor (dimensions in mm).

$\rho_0 = 0.011582$ kg/m^3, and $v_0 = 3400$ m/s, respectively. Since the inlet is designed to result in a temperature of 900 K before the combustion-inducing shock generated by the cowl of the engine, the air properties after the first inlet shock are $p = 4758$ Pa, $T = 462$ K, and $M = 7.73$, which are used as inflow properties at the injector inflow plane. With the fuel inflow stagnation temperature set to 1200 K and the convective Mach number to 1.2 the hydrogen inflow velocity and static temperature are 5257 m/s and 243 K, respectively; its exit pressure is approximately matched to that of the surrounding air. It has thus a global equivalence ratio of 0.82. Figure 3 represents the resulting fuel/air distribution in planes normal to the oncoming flow direction at distances $x = 70$, 80, 90, and 100 cm downstream from the inlet tip, due to very strong vortices generated by the cantilevered ramp injector employed. It can be seen that by a distance $x \sim 85$ cm the fuel/air mixture penetrates the hot boundary layer after the second shock.

In [14] it was shown that under the above considered conditions premature ignition occurs primarily in the boundary layer in the last 15% of the inlet length, spreading into the core flow before the inlet exit. Both gaseous nitrogen and hydrogen were injected into the inlet flowfield, in an attempt to suppress the flame, through wall slots located just before the second inlet shock, as depicted in Fig. 2. In the present paper, the strategy of injecting gaseous hydrogen through a wall slot 5 mm in height, slightly higher than the local boundary layer thickness, positioned just before the second inlet spike ($x = 0.69$ m) is selected [14]. The velocity and temperature of its wall jet are 5257 m/s and 243 K, that is, the same as for the cantilevered injectors with the exception that its pressure is maintained at 6 kPa to match the pressure of the adjacent flow. This results in a global fuel/air equivalence ratio of 1.35 in the inlet. The stagnation temperature and pressure of the wall hydrogen jet are 1216 K and 1571 kPa, respectively. The convective Mach number is unaltered at $M_c = 1.2$.

The combustor consists of an added cowl placed at the inlet exit, with its tip placed at the intersection of the two main inlet shocks (Fig. 4b, point D) and its lower, inner, wall at a certain angle to the approaching inlet flow direction. The reflection corner (Fig. 4b, point G) where the cowl-induced shock intersects the inlet wall is placed such that the center node of the (smeared) shock hits the reflection corner. To prevent sudden expansion and possible separation of the boundary layer as it passes over the reflection corner, the corner is slightly rounded for certain combustor geometries.

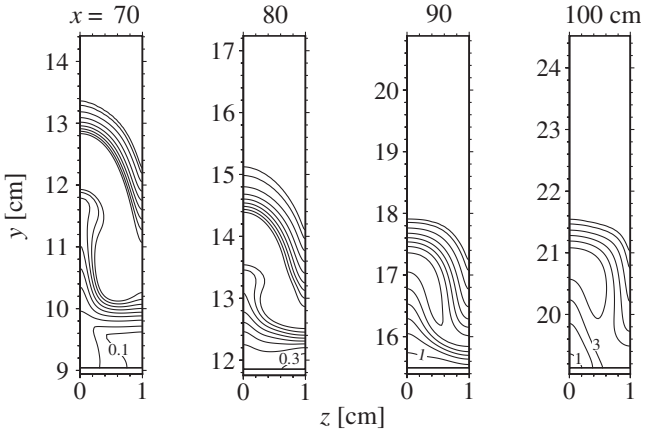

Fig. 3 Equivalence ratio contours in the shock–shock inlet model considered; contour levels at $\phi = 0.1, 0.3, 1, 2, \ldots, 6, 7$.

Governing Equations

The shcramjet flowfield, described by the Favre-averaged Navier–Stokes equations, is closed by the $k\omega$ turbulence model of Wilcox [8] and the 9-species, 20-reaction Jachimowsky H_2-air chemical model [15] (nitrogen is assumed to be an inert gas) and expressed in generalized coordinates as $\partial Q/\partial\tau = -R$ with the residual

$$R = \sum_{i=1}^{d}\left[\frac{\partial F_i}{\partial X_i} - \sum_{j=1}^{d}\frac{\partial}{\partial X_i}\left(K_{ij}\frac{\partial G}{\partial X_j}\right)\right] - S \tag{1}$$

of which a minimization is sought. For the conservative variable, convective flux, and diffusion term, we have

$$Q = \frac{1}{J}\begin{bmatrix}\rho_1\\ \vdots\\ \rho_{n_s}\\ \rho v_1\\ \vdots\\ \rho v_d\\ \rho E\\ \rho k\\ \rho\omega\end{bmatrix} \qquad F_i = \frac{1}{J}\begin{bmatrix}\rho_1 V_i\\ \vdots\\ \rho_{n_s} V_i\\ \rho v_1 V_i + X_{i,1}P^\star\\ \vdots\\ \rho v_d V_i + X_{i,d}P^\star\\ V_i(\rho E + P^\star)\\ \rho V_i k\\ \rho V_i\omega\end{bmatrix} \qquad G = \begin{bmatrix}c_1\\ \vdots\\ c_{n_s}\\ v_1\\ \vdots\\ v_d\\ T\\ k\\ \omega\end{bmatrix} \tag{2}$$

The total energy E and effective pressure $P^\star$ include molecular and turbulent properties, $E = e + k + \frac{1}{2}q^2$ and $P^\star = P + \frac{2}{3}\rho k$, with v_i being the velocity component in the Cartesian x_i direction. The internal energy, enthalpy, and specific heat at constant pressure are determined from temperature dependent polynomials from McBride and Reno [21], whereas P is found through the ideal gas law from the temperature and the density. The diffusion matrix can be shown to correspond to

$$K_{ij}=\frac{1}{J}\begin{bmatrix} \nu_1^\star\alpha_{ij} & \cdots & 0 & 0 & \cdots & 0 & & 0 & 0 & 0 \\ \vdots & \ddots & \vdots & \vdots & \ddots & \vdots & & \vdots & \vdots & \vdots \\ 0 & \cdots & \nu_{n_s}^\star\alpha_{ij} & 0 & \cdots & 0 & & 0 & 0 & 0 \\ 0 & \cdots & 0 & \mu^\star\beta_{ij}^{11} & \cdots & \mu^\star\beta_{ij}^{1d} & & 0 & 0 & 0 \\ \vdots & \ddots & \vdots & \vdots & \ddots & \vdots & \cdots & \vdots & \vdots & \vdots \\ 0 & \cdots & 0 & \mu^\star\beta_{ij}^{d1} & \cdots & \mu^\star\beta_{ij}^{dd} & & 0 & 0 & 0 \\ \nu_1^\star\alpha_{ij}h_1 & \cdots & \nu_{n_s}^\star\alpha_{ij}h_{n_s} & \mu^\star\sum_k\beta_{ij}^{k1}v_k & \cdots & \mu^\star\sum_k\beta_{ij}^{kd}v_k & & \kappa^\star\alpha_{ij} & \mu_k^\star\alpha_{ij} & 0 \\ 0 & \cdots & 0 & 0 & \cdots & 0 & & 0 & \mu_k^\star\alpha_{ij} & 0 \\ 0 & \cdots & 0 & 0 & \cdots & 0 & & 0 & 0 & \mu_\omega^\star\alpha_{ij} \end{bmatrix} \tag{3}$$

where α and β are a function of the metrics only,

$$\alpha_{ij}=\sum_{k=1}^{d}X_{i,k}X_{j,k}$$

and

$$\beta_{ij}^{mn}=\alpha_{ij}\delta_{mn}^{\mathrm{Kr}}+X_{j,m}X_{i,n}-\tfrac{2}{3}X_{j,n}X_{i,m}$$

For the effective viscosity, thermal conductivity, mass diffusion, and diffusion coefficients of the turbulence kinetic energy (TKE) and length scale determining equations, we set $\mu^\star=\mu+\mu_{\mathrm{t}}$,

$$\kappa^\star=\kappa+C_P\frac{\mu_t}{Pr_t}$$

$$\nu_k^\star=\nu_k+\frac{\mu_t}{Sc_t}$$

$$\mu_k^\star=\mu+\frac{\mu_t}{\sigma_k}$$

and

$$\mu_\omega^\star=\mu+\frac{\mu_{\mathrm{t}}}{\sigma_\omega}$$

The molecular diffusion coefficients μ, κ, and ν for each species are determined from polynomials based on the kinetic theory of gases [22]. The viscosity and mass diffusion of the gas mixture are found from Wilke's mixing rule, whereas the thermal conductivity of the mixture is determined from the Mason and Saxena relation. The source term includes the chemical species production terms and the baseline terms of the $k\omega$ model as well as some additional terms needed to account for compressibility effects:

$$S=\frac{1}{J}\begin{bmatrix} \dot{W}_1 \\ \vdots \\ \dot{W}_{n_s} \\ 0 \\ \vdots \\ 0 \\ P_k-\rho\varepsilon-\rho\varepsilon f(M_t) \\ \frac{\omega}{k}\left(\frac{5}{9}P_k-\frac{5}{6}\rho\varepsilon\right)+\rho\omega^2 f(M_t) \end{bmatrix} \tag{4}$$

where n_s is the number of species involved in the chemical reaction, and $\varepsilon\equiv k\omega$. The dilatational dissipation correction terms [that is, the ones involving $f(M_t)$] are necessary to account for the reduced growth of shear layers when the convective Mach number is high [23,24]. The Wilcox [9] dilatational dissipation model specifies $f(M_t)$ as $f(M_t)=\frac{3}{2}\max(0,M_t^2-1/16)$. This improves the baseline $k\omega$ equations in solving high convective Mach number shear layers without underpredicting the skin friction in high Mach number boundary layers, at least up to a freestream Mach number of 6. More compressibility corrections exist [25–27], but due to very little or no empirical data to justify their presence their effect is neglected in the present study. Based on dimensional analysis arguments, the turbulent viscosity μ_t can be written as $\mu_t=0.09\frac{\rho k}{\omega}$ from which the effective viscosity can be determined as $\mu^\star=\mu+\mu_t$. From the exact form of the transport equation for k, the turbulence kinetic energy production term can be written in generalized coordinates as

$$P_k=\sum_{i=1}^{d}\sum_{j=1}^{d}\left(-\frac{2}{3}\rho kX_{i,j}\frac{\partial v_j}{\partial X_i}+\sum_{m=1}^{d}\sum_{n=1}^{d}\mu^\star\beta_{ij}^{mn}\frac{\partial v_m}{\partial X_i}\frac{\partial v_n}{\partial X_j}\right) \tag{5}$$

Finally, the turbulent Prandtl number, σ_k, and σ_ω are set to 0.9, 2.0, and 2.0, respectively, while the turbulent Schmidt number is set to 1.0, and not altered in space.

Numerical Method

All partial derivatives are discretized using centered finite difference second-order accurate stencils except for the convection derivative, which is discretized using the approximate Riemann solver of Roe [28] and made second order accurate through a symmetric minmod limiter by Yee et al. [29]. The discretized residual is solved to steady state using a block-implicit approximate factorization algorithm [30,31] including the analytical Jacobian derived from the chemical model and a linearization strategy of the viscous terms by Chang and Merkle [32]:

$$\prod_{i=1}^{d}\left[I+\Delta\tau\overline{\delta_{X_i}A_i}-\Delta\tau C_i^-\right]-\Delta\tau\sum_{j=1}^{d}\delta_{X_i}(K_{ij}\delta_{X_j}B)\Delta Q=-\Delta\tau R_\Delta \tag{6}$$

with B the linearization Jacobian of the viscous terms ($B\equiv\partial G/\partial Q$) and C_i^- the linearization Jacobian of the negative source terms ($\partial S^-/\partial Q$) for the $i=1$ sweep but ignored for the other sweeps. Only the negative source terms are linearized to ensure the stability of the implicit algorithm [33]. The term $\overline{\delta_{X_i}A_i}$ is symbolic and stands for the linearization of the first-order Roe scheme with the Roe Jacobian locally frozen [34,35]. Although more costly per iteration compared to an LUSGS (lower–upper symmetric Gauss–Seidel) inversion strategy, approximate factorization is chosen here for its ability to solve the Roe scheme without the need of introducing an explicit artificial dissipation term in the residual (the entropy correction) to stabilize the iterative process. The introduction of the entropy correction can lead to excessive artificial dissipation, which affects the accuracy of the solution considerably [3].

Convergence is reached when ξ for all nodes falls below a user-defined threshold value, ξ_{verge}. We choose to define ξ as the

summation of the discretized continuity and energy conservation equation residuals weighted by J^{-1}:

$$\xi \equiv \frac{J}{\rho}\sum_{k=1}^{n_s}|R_{\Delta k}| \tag{7}$$

The pseudotime step $\Delta\tau$ is fixed to the geometric average between the minimum and maximum Courant–Friedrichs–Lewy (CFL) conditions, which is found to give faster convergence than the minimum CFL condition for cases involving high mesh aspect ratios.

Boundary Conditions

The computational domain extends (see Figs. 2 and 4) in the x-longitudinal direction, from $x = 0$, the inlet tip, to $x = 1.4$ m, the end of the combustor section; in the y-vertical direction, from $y = 0$ at the lower wall surface, to either $y = 31.0$ cm or $y = 28.8$ cm (depending on the flow-turning angle), the top boundary consisting of a free surface, AB, is approximately parallel to the incident shock generated by the inlet wedge. The incident angle of the upper free surface is reduced above the H_2 slot injector, at point B, ending at a point slightly above the cowl tip, at point C. In the combustor, the upper surface is formed by the cowl inner surface, DE. Because of the symmetry of the "infinite" injector arrays in the lateral z direction, the computational domain is bounded by $z = 0$, the injector symmetry plane, and by $z = D_{\text{array}}/2 = 1$ cm. The left and top free-surface boundaries of the computational domain are set to supersonic inflow, with the right boundary set to supersonic outflow. Second-order accurate, symmetric boundary conditions are imposed on the sides of the computational domain, that is, an extrapolating polynomial of the form

$$\psi^X = \tfrac{4}{3}\psi^{X+1} - \tfrac{1}{3}\psi^{X+2} \tag{8}$$

is used to obtain $P^\star$, ρ, k, ω, and the velocity component tangent to the surface, while the perpendicular velocity component is set to zero. At the walls, the velocity and turbulence kinetic energy are fixed to zero, the pressure is extrapolated using the above polynomial form, the temperature is set, in all cases, to 500 K, and the turbulence dissipation rate is specified as $\omega_W = 36\mu/5\rho d_W^2$, d_W being the distance between the near wall node and the wall. A short 5 mm long runway (Fig. 1) is imposed on the fuel jet before injection to avoid a singularity in the turbulence and other flow properties at the start of the mixing layer; this also reduces the solution sensitivity to the freestream value of ω which is set [36] to $10q_\infty/L$ ($L = 1$ m). In the Wilcox $k\omega$ model used here, the turbulence kinetic energy is set to a small value in the freestream to prevent a division by zero in the dissipation rate source term, Eq. (4). However, in the present study, the freestream value of k is set to zero, that is, $k = 0$ at the inflow boundary and $\tilde{k}$ is defined as

$$\tilde{k} = \max\left[k, \min\left(k_{\text{div}}, \frac{\omega\mu}{\rho}\right)\right] \tag{9}$$

with k_{div} a user-specified constant which is generally set lower than one-tenth of the maximum value of k throughout the boundary layer [10]. This is verified numerically not to affect the laminar sublayer but to improve the robustness and efficiency of the integration significantly. The minimum between k_{div} and $\omega\mu/\rho$ is taken so that a clipping occurs *only* in nonturbulent flow regions in which an accurate representation of ω does not affect the accuracy of the flowfield. A value of k_{div} of 1×10^3 m^2/s^2 is used for all cases and is verified to be below the maximum value of k in the boundary layer which for the present case is typically 6×10^4 m^2/s^2, and reaches a minimum of 2×10^4 m^2/s^2 at $x = 1.18$ m.

The discretized governing equations together with the boundary conditions are solved on a generalized structured mesh using the (WARP code. A detailed description of the computational technique employed in the WARP code, together with the solution convergence and streamwise ellipticity criteria used, is given in [10]. It contains a new convergence acceleration technique for streamwise-separated hypersonic flow, dubbed the "marching window," which decreases 10–20 fold the computing time and the memory required by 5 times. This permits the solution of significantly finer meshes and, hence, results in a decreased numerical error.

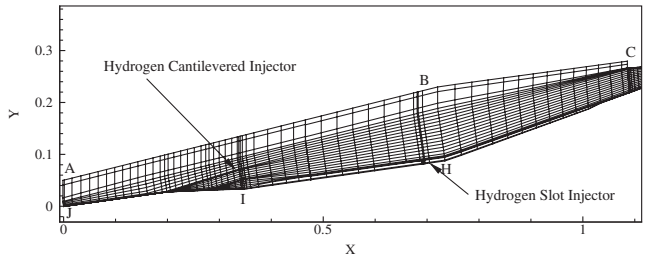

a) Inlet mesh

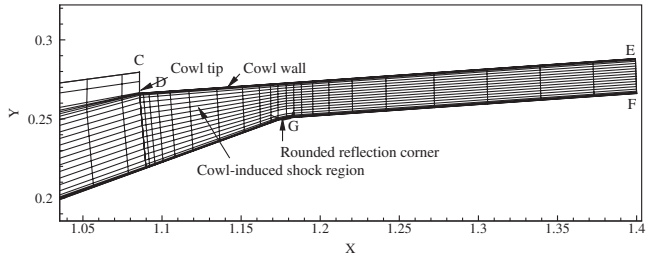

b) Combustor mesh

Fig. 4 Sample mesh fitting the inlet and combustor geometry in the plane $z = 0$ m. Every tenth grid line is shown.

Efficiency Measures

The concept of thrust potential [6,37] is used to assess the effectiveness of the considered shcramjet model as a hypersonic propulsion device. This concept is directly linked to the reversible (ideal) engine thrust via all irreversible engine flow losses. The thrust potential, at a certain x-station b in the engine, is defined as the thrust that would be obtained if the flow is *reversibly* expanded downstream of station b to a specified engine exit area. A detailed derivation of the expression for the thrust potential

$$\boldsymbol{F}_{\text{pot}} = -\boldsymbol{F}_{\text{pot,ref}} + \int_b \frac{\rho_c q_c^2 + P_c^\star}{\rho_c q_c}\,\mathrm{d}\dot{m}/\dot{m}_{\text{air,engine}} \tag{10}$$

is given in [6]. Here the flow properties assigned the subscript c are reversibly expanded from station b to an iteratively determined backpressure which is such that the sum of the cross sections of all stream tubes at station c corresponds to the engine inlet area. The reference thrust potential $\boldsymbol{F}_{\text{pot,ref}} = 3420.5$ Ns/kg, so that the thrust potential is zero at the inlet entrance.

The measure of efficiency of the fuel/air mixing process in the inlet of the engine is here quantified by the concept of mixing efficiency [6,38]. In the present study an air-based mixing efficiency, η_m, at an x-station b is used and is defined as the ratio of the mass flux of oxygen that would react (when the mixture temperature is above the ignition point) to the mass flux of oxygen entering the engine:

$$\eta_m \equiv \int_b c_{\text{O}_2}^R\,\mathrm{d}\dot{m}/0.235 \times \dot{m}_{\text{air,engine}} \tag{11}$$

where the mass fraction of reacting oxygen, $c_{\text{O}_2}^R$, is given by

$$c_{\text{O}_2}^R = \min\left(c_{\text{O}_2}, c_{\text{O}_2}^S c_{\text{H}_2}/c_{\text{H}_2}^S\right) \tag{12}$$

with the stoichiometric mass fraction of hydrogen $c_{\text{H}_2}^S = 0.02876$, and the stoichiometric mass fraction of oxygen $c_{\text{O}_2}^S = 0.22824$.

The friction force on the internal surfaces of the shcramjet is taken as the negative of the viscous momentum flux entering the computational domain at the surfaces

$$\boldsymbol{F}_{\text{skin friction}} = \frac{1}{\dot{m}_{\text{engine}}} \sum_{\text{surface nodes}} \Delta X_i \left[\sum_{j=1}^{d} K_{i,j} \frac{\partial G}{\partial X_j} \right] \tag{13}$$

Only the momentum components of the vector in the right-hand side of Eq. (13) are considered. Here X_i is the curvilinear coordinate perpendicular to the body surfaces and ΔX_i is the spacing in the computational domain between the boundary node and the closest inner node. The friction force is normalized by $\dot{m}_{\text{engine}}$ which corresponds to the sum of the air and injected fuel mass flow rates entering the shcramjet inlet. This is done to readily compare the normalized skin friction losses to thrust potential gains and losses. The friction force in the flight direction is the x component of the above vector.

Grid Convergence

The standard grids employed in the inlet and combustor are shown in Figs. 4a and 4b, respectively. In the inlet (fuel/air mixing region) of computational domain dimensions 109 cm × 27.8 cm × 1 cm, the mesh is uniformly spaced in the streamwise coordinate x and spanwise coordinate z. Along the lateral coordinate y, the mesh exponentially grows from a specified wall node spacing of 10 μm to a uniform spacing in the mixing region. This results in a value of y^+ at the wall of the inlet ranging typically from 1 to 3, with the maximum observed at the inlet exit. Before the mixing region, JI (on the initial 8 deg wedge and injector surfaces), the wall node spacing is set to 30 μm with the corresponding y^+ values ranging from 1 to 3. The cowl and combustor duct are added to the resulting inlet grid. In the combustor of computational domain dimensions 31 cm × 4.6 cm ×1 cm, the grid is evenly spaced in the z direction with $\Delta z = 0.27$ mm, and clusters in the x direction from 20 μm at the combustor entrance plane to 40 μm at the reflection corner, G. In the y direction, the mesh clusters exponentially to 10 μm at both the inlet wall and the cowl surfaces, resulting in a value of $y^+ = 4$ at the combustor exit. The total number of nodes used for the entire inlet-combustor combination for the standard grid is approximately 5.4×10^6, which results in a slightly higher grid density in the combustor than in the inlet. Convergence is reached when $\xi \leq \xi_{\text{verge}}$ for all inner nodes, with the user-defined convergence criterion ξ_{verge} set to 4×10^2 1/s for all inlet cases, which has been shown to be sufficient for a similar problem [3]. Details on the definition of ξ can be found in [10]. The streamwise ellipticity sensor threshold φ_{verge} is set to 7×10^4 1/s. No entropy correction term is used in the Roe scheme in the considered flowfield, to avoid an excess in numerical dissipation, which would increase the grid-induced error [3].

To assess the error originating from the standard grid employed, three other mesh levels were computed and the solutions compared. They correspond to mesh dimension factors $r = 0.67$, $r = 1.50$, and $r = 2.25$, the standard grid corresponding to a mesh dimension factor $r = 1.0$. The quantity r is a factor that multiplies the mesh in each dimension. Note that the ratios of dimension factors between successive grids is left constant. Such a strategy, as opposed to setting a constant Δr between meshes, translates into a more rigorous grid-convergence study. A grid-convergence analysis was performed only for the combustor portion, as previous studies have examined the shcramjet inlet extensively [12]. For the combustor duct, the 12 deg flow-turning angle case was chosen to maximize the resulting changes in the combustion process, due to the large ignition delay present for this case. The overall combustor mesh sizes were 0.5, 1.7, 5.9, and 19.2 million nodes, for the cases of $r = 0.67$, 1.0, 1.5, and 2.25, respectively.

Figures 5a and 5b show the grid-convergence results for the mixing efficiency and thrust potential performance parameters, respectively. As can be seen from both figures, the standard grid density represented by $r = 1.0$ approaches the converged value with only a minor grid-induced error. In both cases, the grid density represented by $r = 1.5$ overshoots the converged value, partially returning toward the standard grid density values for the highest grid density used, represented by $r = 2.25$. This indicates that the standard mesh density employed, for $r = 1.0$, provides acceptable

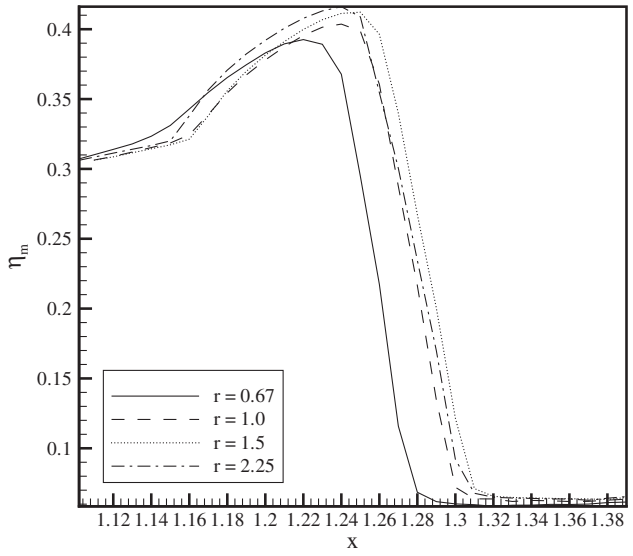

a) Grid convergence of mixing efficiency, η_m

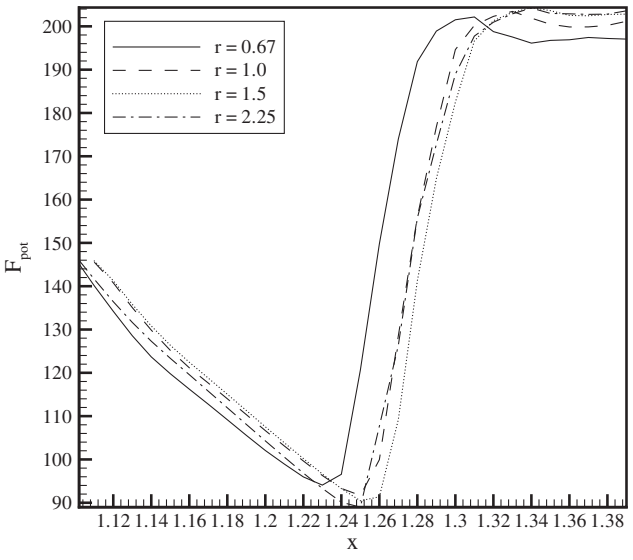

b) Grid convergence of thrust potential, F_{pot}

Fig. 5 Grid-convergence results for flowfield performance parameters.

results. Similar results are obtained when comparing the resultant ignition delays. From the standard mesh case, an ignition delay of 10.5 cm is obtained. This increases to 10.9 cm for the next highest grid density, but is then reduced to 10.8 cm for the highest grid density.

Combustor Flowfield Analysis

Combustion of the premixed inlet flow was induced through the shock wave generated by the cowl of the engine. Two cowl angle settings of 8 and 4 deg with respect to the oncoming flow direction were considered (Fig. 2), corresponding to inlet flow-turning angles of 12 and 16 deg, respectively.

The resulting shock-induced combustion flowfield characteristics, in the injector symmetry plane, $z = 0$, are shown in Figs. 6–8. A sizable ignition delay of approximately 10.5 cm is visible in Fig. 6a behind the cowl-induced shock for the inlet flow-turning angle of 12 deg. The lower cowl angle setting of 4 deg reduces this ignition delay to 4.5 cm. In both cases, combustion occurs rapidly and water mass fractions, Fig. 7, reach, approximately, the maximum equilibrium value. Note the region of pure air in the upper portion of the combustor duct which does not contribute to heat release due to incomplete fuel/air mixing. The pressure field generated by the

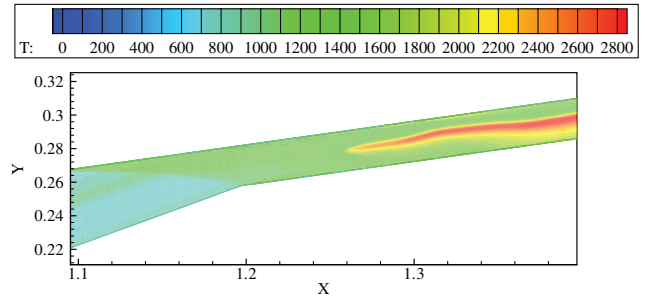

a) 12° inlet flow-turning angle

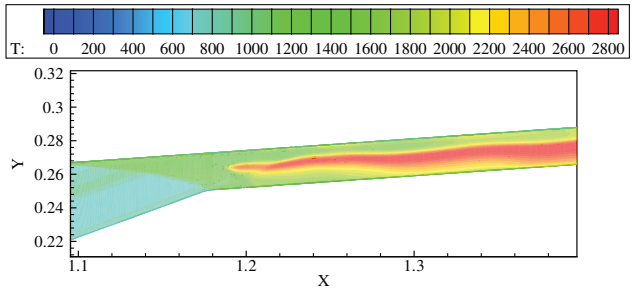

b) 16° inlet flow-turning angle

Fig. 6 Temperature contours in the combustor duct in the plane $z = 0$ m.

combustion process is depicted in Fig. 8. In both cases compression waves are formed at the tip of the upper flame boundary, and immediately behind the lower flame front near the wall, which then reflect from the walls of the combustor duct and are responsible for the slightly wavy structure of the upper flame surface (Fig. 6). The weak, curved compression wave emanating from point C, Fig. 8b, for the 16 deg turning angle, is due to a small recirculation region formed at the intersection of the cowl-generated shock with the inlet wall boundary layer. This small recirculation region increased significantly in size when the inlet flow was subjected to a 20 deg turning angle, due to a stronger shock-induced combustion wave.

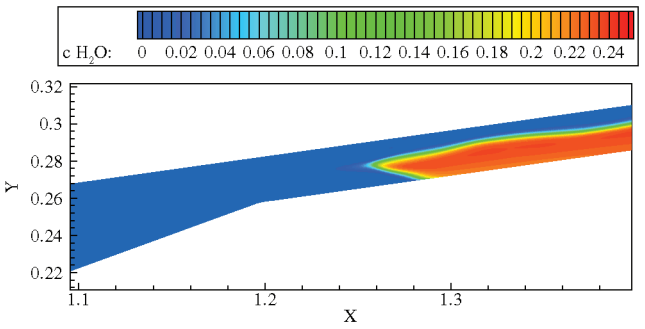

a) 12° inlet flow-turning angle

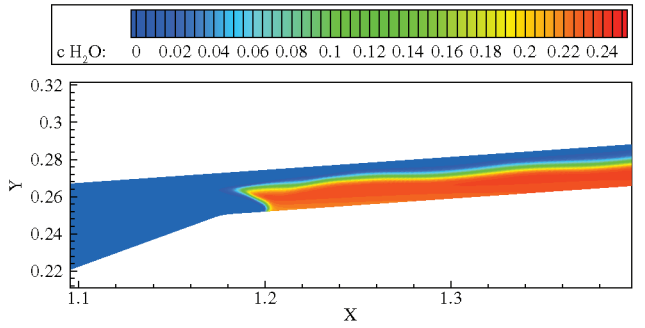

b) 16° inlet flow-turning angle

Fig. 7 H_2O mass-fraction contours in the combustor duct in the plane $z = 0$ m.

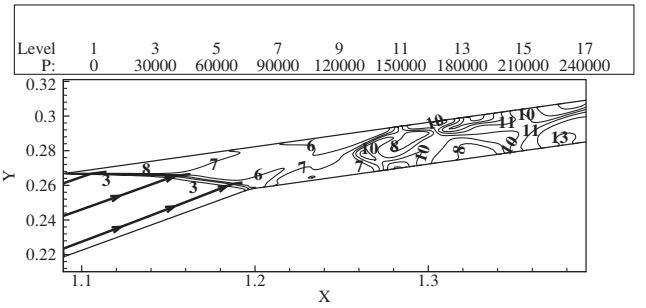

a) 12° inlet flow-turning angle

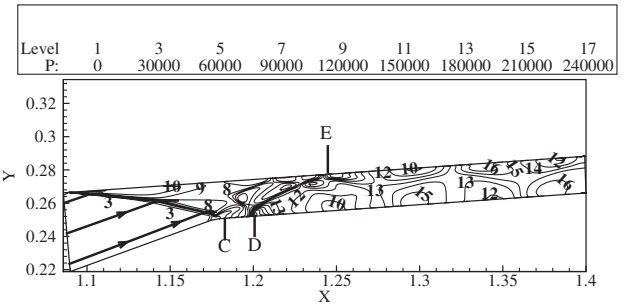

b) 16° inlet flow-turning angle

Fig. 8 Pressure field contours in the combustor duct in the plane $z = 0$ m.

The development and propagation of the combusting region in the lateral (y, z) plane is presented in Fig. 9 as water mass-fraction contours, with overlaid O_2 mass-fraction contours, in successive $x =$ const planes in the combustor. It can be seen that ignition begins in the region between the cantilevered injectors and also in the small region formed at point C, Figs. 8b and 9b. The flame spreads first from one injector to the next in the lateral z direction, and then downward, until it envelops the entire lower region of the duct.

Figures 9a and 9b both indicate an absence of oxygen in the middle and lower regions of the combustor duct. For Figs. 10 and 11, Y_n represents the distance above the lower duct wall normalized by the overall duct height. As can be seen, a certain amount of hydrogen still remains in the lower region of the duct (Fig. 10), but the reaction

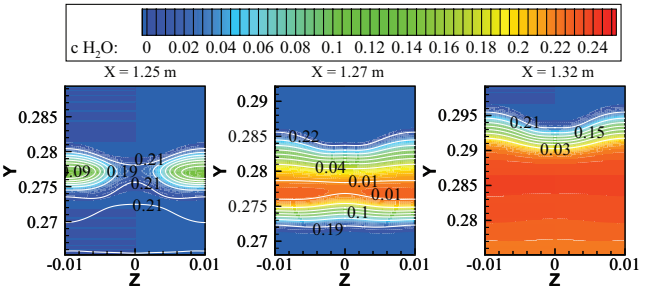

a) 12° inlet flow-turning angle

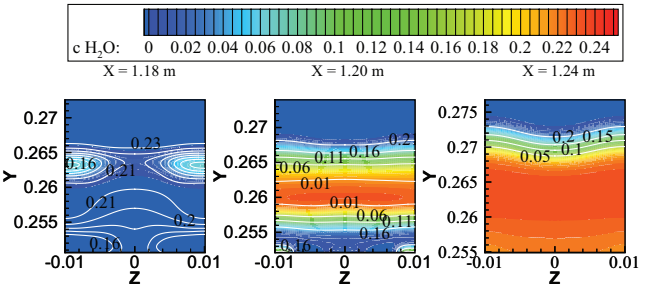

b) 16° inlet flow-turning angle

Fig. 9 H_2O contour (O_2) plots in $x =$ const planes along the combustor.

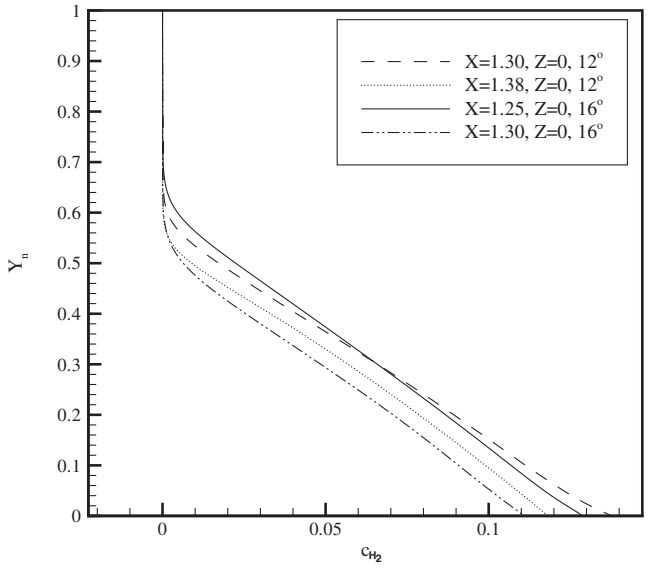

Fig. 10 Variations of fuel mass fraction H_2 in $x = \text{const}$ planes.

cannot proceed any further due to the absence of oxygen. In both cases, the combustion proceeds to the same degree of completion; a stronger shock-induced combustion wave would only serve to reduce the resulting ignition distance. Examination of the mass fraction of OH, Fig. 11, reveals that the ignition process is strongest in the upper portion of the shock-induced combustion wave and at the interface between fuel and air in the upper region of the combustor duct.

Figures 12–14 depict the variations of pressure, temperature, and fuel mass fraction along three stream traces, beginning in the $z = 0$ plane, for the 16 deg inflow flow-turning angle, dubbed lower, middle, and upper region stream traces (see Fig. 8). It can be seen, Fig. 12, that the pressure is maximum near the wall region, in the vicinity of point D on the lower combustor duct wall, and also at point E, on the upper duct wall where the compression wave generated at point D, at the start of the flame front, reflects from the upper combustor wall. The pressure rises through the cowl-generated shock, is constant throughout the induction zone for the middle stream trace passing through the shock-induced combustion zone, and increases when it passes through the combustion wave. The "sinusoidal" variation of the pressure along the lower region stream trace, subsequent to its increase through the cowl-generated shock, is

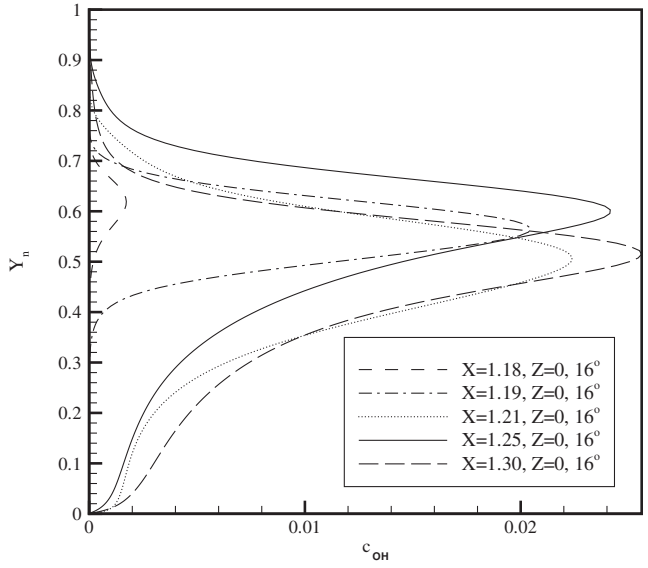

Fig. 11 Variations of OH mass fraction in $x = \text{const}$ planes for an inlet flow-turning angle of 16 deg.

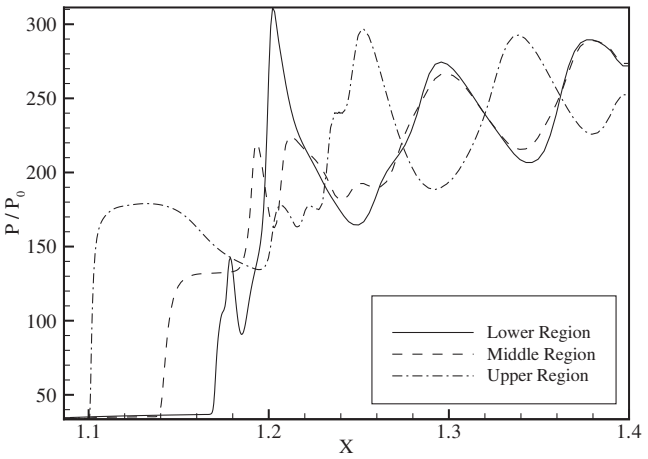

Fig. 12 Pressure along stream traces for a 16 deg inlet flow-turning angle.

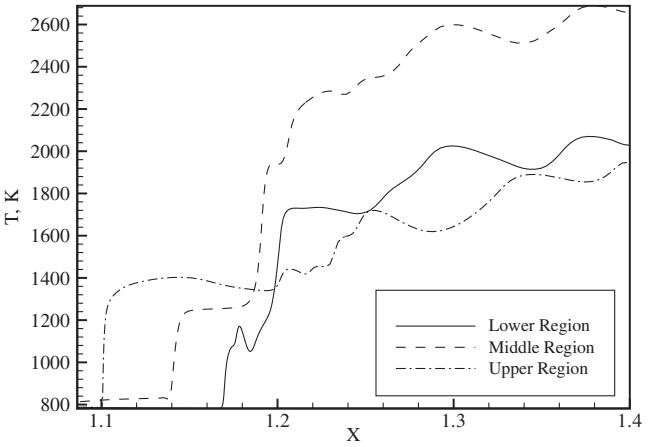

Fig. 13 Temperature along stream traces for a 16 deg inlet flow-turning angle.

due to a small recirculation region in the vicinity of point C of the lower combustor wall (Fig. 8b). The temperatures along these three stream traces, Fig. 13, increase through the cowl shock and through the combustion front. The maximum temperature of approximately 2688 K is reached in the middle region of the combustor by the end of the computational domain. Fuel mass-fraction variations along the lower region stream trace, Fig. 14, increase due to slot-injected hydrogen near the wall, decrease after crossing the cowl shock and the flame front, and continue to decrease near the lower wall region of

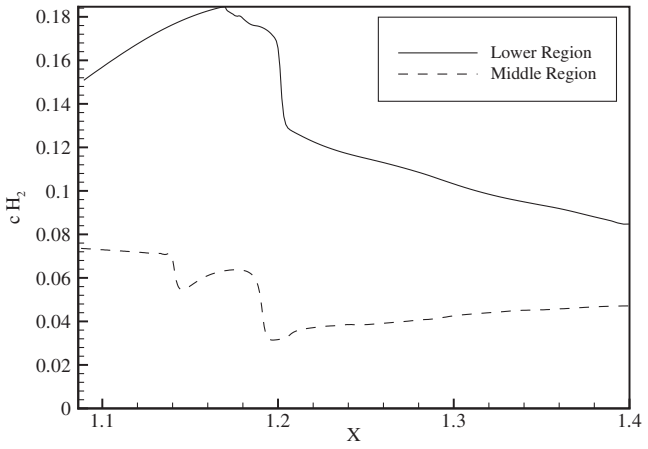

Fig. 14 H_2 mass fraction along stream traces for a 16 deg inlet flow-turning angle.

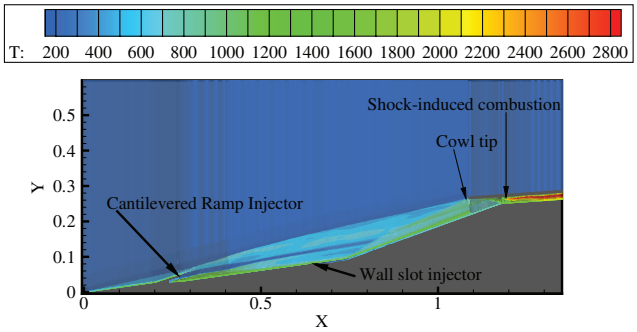

Fig. 15 Temperature contours in a real shcramjet flowfield for a 16 deg inlet flow-turning angle in the $z = 0$ plane.

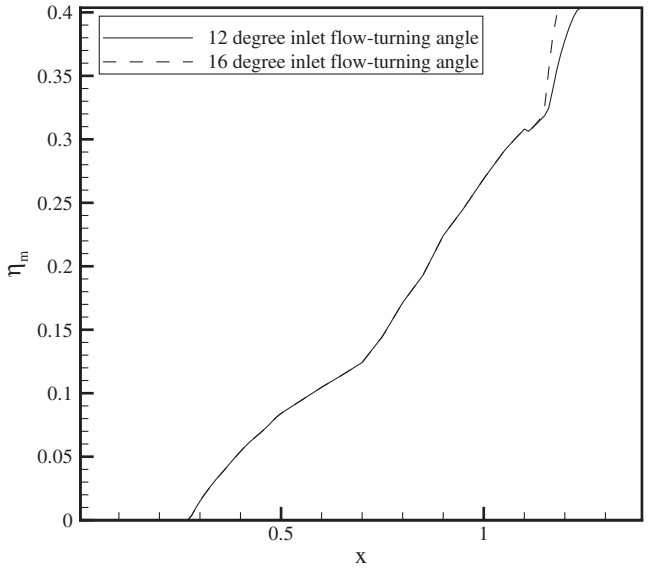

Fig. 16 Mixing efficiency, η_m, variation along the shcramjet for 12 and 16 deg inlet flow-turning angles.

the duct due to subsequent flowfield development. In the middle region of the combustor flow, the H_2 mass fraction decreases then increases slightly through the cowl shock and then decreases across the flame front. The mass fraction then slowly increases in the remainder of the combustor duct, again due to subsequent flow development.

Figure 15 represents the combined inlet-combustor flowfield configuration as temperature contour plots of a real shcramjet in the $z = 0$ plane and for a 16 deg inlet flow-turning angle. Clearly visible are the injected fuel trajectory and the shock-induced combustion process.

Shcramjet Performance

The shcramjet performance characteristics are assessed by the air-based mixing efficiency, Eq. (11), the concept of thrust potential, Eq. (10), and by frictional forces, Eq. (13), which are determined as the negative of the x component of the viscous momentum flux entering the computational domain at all surfaces of the shcramjet (except the external cowl surface). Note that frictional forces are normalized by the total mass flow rate entering the shcramjet inlet to allow a comparison between the thrust potential gains/losses and losses due to friction.

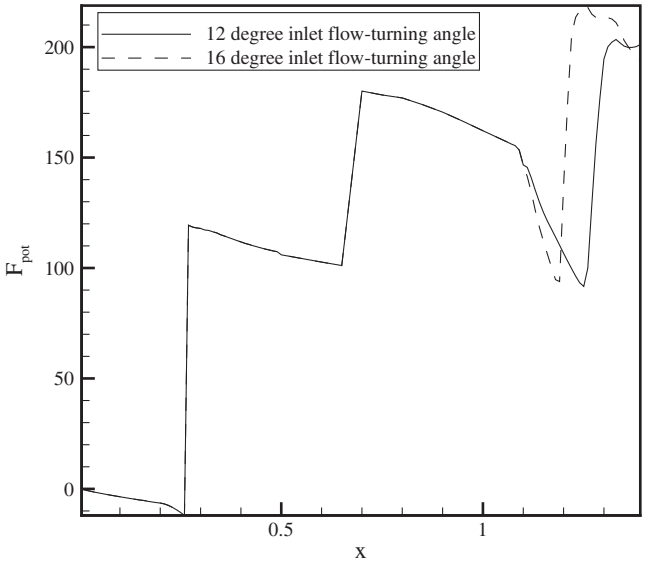

Fig. 17 Thrust potential, F_{pot}, variation along the shcramjet for 12 and 16 deg inlet flow-turning angles.

The mixing efficiency variation throughout the inlet and combustor for the two inlet flow-turning angles considered is depicted in Fig. 16. For both cases the mixing efficiency increases continuously to a value of approximately 0.31 just before the cowl-generated shock. Note the large increase of approximately 30% in the mixing efficiency produced by the cowl shock, resulting in a final air-based mixing efficiency of 41% before ignition. The corresponding variation of the thrust potential of the shcramjet is shown in Fig. 17. In both considered cases, considerable gains in thrust potential are due to the fuel being injected at a high speed by the cantilevered ramp injector and through the wall slot, necessary to cool the boundary layer and suppress premature ignition in the inlet flow. The thrust potential increases sharply due to shock-induced combustion. The thrust potentials reach their maximum values of 203.4 and 218.8 Ns/kg after only 22 and 14 cm from the combustor entry plane for the 12 and 16 deg turning angles, respectively, resulting in a very short combustor. Table 1 shows the respective thrust potential gains and losses in the entire inlet-combustor section of the shcramjet. Note that the thrust potential gain/loss ratios are 2.65 and 2.44, respectively. The fuel specific impulse of the considered inlet-combustor shcramjet model is calculated by

$$I_f = \frac{\max \boldsymbol{F}_{\text{pot}} \cdot \dot{m}_{\text{air,engine}}}{g\dot{m}_j} = \frac{\max \boldsymbol{F}_{\text{pot}}}{gf_s\phi} = \frac{\max \boldsymbol{F}_{\text{pot}}}{gf_s \cdot 1.35} \tag{14}$$

where $g = 9.81$ m/s^2, the gravitational constant. The resulting values are given in Table 1. Increasing the inlet flow-turning angle from 12 to 16 deg, that is, generating stronger shock-induced combustion waves, increases the magnitude of the I_f only by 7%. The magnitude of frictional forces acting on the entire inlet-combustor surface is 149.4 Ns/kg for the 12 deg inlet flow-turning angle, and 184.5 Ns/kg for the 16 deg inlet flow-turning angle. Frictional forces acting on the internal duct surfaces of the combustor alone constitute a very significant fraction of the total frictional forces. Note that the frictional force acting in the inlet alone is 36.8 Ns/kg.

Table 1 Tabulated shcramjet performance parameters

Case	$\boldsymbol{F}_{\text{pot}}$ gains, Ns/kg	$\boldsymbol{F}_{\text{pot}}$ losses, Ns/kg	max $\boldsymbol{F}_{\text{pot}}$, Ns/kg	I_f, s
12 deg inlet flow-turning angle	318.5	−120.3	203.4	532.7
16 deg inlet flow-turning angle	333.0	−136.6	218.8	573.1

Concluding Remarks

It has been shown, by numerical simulation, that the concept of a shock-induced combustion ramjet is feasible, that is, the fuel/air mixing can be organized in the inlet of the hypervelocity vehicle and, in certain conditions, to suppress the undesired premature ignition of the combustible mixture in the boundary layer of the inlet wall. The combustor length resulting from the shock-induced combustion process is, indeed, very short, of the order of 30% of the inlet length. Stronger shock-induced combustion waves do not appreciably increase the level of heat addition or the thrust potential of the engine; they rather decrease the induction distance of the chemical reaction process. However, the interaction of strong shock-induced combustion waves with the inlet boundary layer result in extended and strong recirculation zones that degrade the performance of the inlet-combustor system. The performed analysis demonstrates the primary role of the fuel/air mixing process in the propulsive performance of the shcramjet. Indeed, the relatively low values of the fuel specific impulse obtained are mainly due to incomplete mixing achieved in the adopted external, two-oblique shock wave compression inlet model, due to the second inlet shock compressing further the fuel/air mixing zone towards the wall of the inlet. Other shcramjets should be considered to further improve the fuel specific impulse of the engine.

Acknowledgment

This work has been supported by the National Sciences and Engineering Research Council (NSERC).

References

[1] Sislian, J. P., "Detonation Wave Ramjets," *Scramjet Propulsion*, edited by E. T. Curran and S. N. B. Murthy, Vol. 189, Progress in Aeronautics and Astronautics, AIAA, Washington, D.C., 2001, Chap. 13, pp. 823–889.

[2] Sislian, J. P., and Schumacher, J., "A Comparative Study of Hypersonic Fuel/Air Mixing Enhancement by Ramp and Cantilevered Ramp Injectors," AIAA 99-4873, Nov. 1999.

[3] Parent, B., Sislian, J. P., and Schumacher, J., "Numerical Investigation of the Turbulent Mixing Performance of a Cantilevered Ramp Injector," *AIAA Journal*, Vol. 40, No. 8, 2002, pp. 1559–1566.

[4] Waitz, I. A., Marble, F. E., and Zukoski, E. E., "Vorticity Generation by Contoured Wall Injectors," AIAA Paper 92-3550, 1992.

[5] Mays, R. B., Thomas, R. H., and Schetz, J. A., "Low Angle Injection into a Supersonic Flow," AIAA Paper 89-2461, July 1989.

[6] Parent, B., and Sislian, J. P., "Effect of Geometrical Parameters on the Mixing Performance of Cantilevered Ramp Injectors," *AIAA Journal*, Vol. 41, No. 3, 2003, pp. 448–456.

[7] Parent, B., and Sislian, J. P., "Impact of Axial Vortices on Mixing at a High Convective Mach Number," *AIAA Journal*, Vol. 41, No. 7, 2003, pp. 1386–1388.

[8] Wilcox, D. C., "Reassessment of the Scale Determining Equation for Advanced Turbulence Models," *AIAA Journal*, Vol. 26, No. 11, 1988, pp. 1299–1310.

[9] Wilcox, D. C., "Dilatation-Dissipation Corrections for Advanced Turbulence Models," *AIAA Journal*, Vol. 30, No. 11, 1992, pp. 2639–2646.

[10] Parent, B., and Sislian, J. P., "The Use of Domain Decomposition in Accelerating the Convergence of Quasihyperbolic Systems," *Journal of Computational Physics*, Vol. 179, No. 1, 2002, pp. 140–169.

[11] Parent, B., and Sislian, J. P., "Validation of the Wilcox k-Omega Model for Flows Characteristic to Hypersonic Airbreathing Propulsion," *AIAA Journal*, Vol. 42, No. 2, 2004, pp. 261–270.

[12] Sislian, J. P., and Parent, B., "Hypervelocity Fuel/Air Mixing in a Shcramjet Inlet," *Journal of Propulsion and Power*, Vol. 20, No. 2, 2004, pp. 263–272.

[13] Parent, B., and Sislian, J. P., "Hypersonic Mixing Enhancement by Compression at a High Convective Mach number," *AIAA Journal*, Vol. 142, No. 4, 2004, pp. 787–795.

[14] Schwartzentruber, T. E., Sislian, J. P., and Parent, B., "Suppression of Premature Ignition in the Premixed Inlet Flow of a Shcramjet," *Journal of Propulsion and Power*, Vol. 21, No. 1, 2005, pp. 87–94.

[15] Jachimowsky, C. J., "An Analytical Study of the Hydrogen-Air Reaction Mechanism With Application To Scramjet Combustion," NASA TP 2791, 1988.

[16] Vasilev, V. I., Zolotenko, S. N., Krasheninnikov, S. J., and Stepanov, V. A., "Numerical Investigation of Mixing Augmentation Behind Oblique Shock Waves," *AIAA Journal*, Vol. 32, No. 2, 1994, pp. 311–316.

[17] Livingston, T., Segal, C., Schindler, M., and Vinogradov, V. A., "Penetration and Spreading of Liquid Jets in an External-Internal Compression Inlet," *AIAA Journal*, Vol. 38, No. 6, 2000, pp. 989–994.

[18] Owens, M., Mullagiri, S., Segal, C., and Vinogradov, V. A., "Effects of Fuel Preinjection on Mixing in Mach 1.6 Airflow," *Journal of Propulsion and Power*, Vol. 17, No. 3, 2001, pp. 605–610.

[19] Gouskov, O. V., Kopchenov, V. I., Lomkov, K. E., and Vinogradov, V. A., "Numerical Research of Gaseous Fuel Preinjection in Hypersonic Three-Dimensional Inlet," *Journal of Propulsion and Power*, Vol. 17, No. 6, 2001, pp. 1162–1169.

[20] Bezgin, I., Ganjhelo, A., Gouskov, O., and Kopchenov, V., "Some Numerical Investigation Results of Shock-Induced Combustion," AIAA Paper 98-1513, April 1998.

[21] McBride, B. J., and Reno, M. A., "Coefficients for Calculating Thermodynamic and Transport Properties of Individual Species," NASA TM 4513, Oct. 1993.

[22] Dixon-Lewis, G., "Computer Modelling of Combustor Reactions," *Combustion Chemistry*, edited by W. C. Gardiner, Springer–Verlag, New York, 1984.

[23] Papamoschou, D., and Roshko, A., "The Compressible Turbulent Shear Layer: An Experimental Study," *Journal of Fluid Mechanics*, Vol. 197, 1988, pp. 453–477.

[24] Dimotakis, P. E., "Turbulent Mixing and Combustion," *High-Speed Flight Propulsion Systems*, edited by S. N. B. Murthy and E. T. Curran, Vol. 137, Progress in Aeronautics and Astronautics, AIAA, Washington, D.C., 1991, Chap. 5.

[25] Sislian, J. P., "Equations of Motion and Two-Equation Turbulence Model for Plane or Axisymmetric Turbulent Flows in Body-Oriented Orthogonal Curvilinear Coordinates and Mass- Averaged Dependent Variables," NASA CR 3025, Jan. 1978.

[26] Krishnamurty, V. S., "Effect of Compressibility on the Turbulence Structure and Its Modelling," Ph.D. Dissertation, Department of Aerospace Engineering, Mechanics & Engineering Science, Univ. of Florida, Gainesville, FL, Dec. 1996.

[27] Coakley, T. J., Horstman, C. C., Marvin, J. G., Viegas, J. R., Bardina, J. E., Huang, P. G., and Kussoy, M. I., "Turbulence Compressibility Corrections," NASA TM 108827, May 1994.

[28] Roe, P. L., "Approximate Riemann Solvers, Parameter Vectors, and Difference Schemes," *Journal of Computational Physics*, Vol. 43, No. 2, 1981, pp. 357–372.

[29] Yee, H. C., Klopfer, G. H., and Montagné, J.-L., "High-Resolution Shock-Capturing Schemes for Inviscid and Viscous Hypersonic Flows," *Journal of Computational Physics*, Vol. 88, No. 1, 1990, pp. 31–61.

[30] Douglas, J., Jr., "On the Numerical Integration of $\partial^2 u/\partial x^2 + \partial^2 u/\partial y^2 = \partial u/\partial t$ by Implicit Methods," *Journal of the Society for Industrial and Applied Mathematics*, Vol. 3, No. 1, 1955, pp. 42–65.

[31] Peaceman, D. W., and Rachford, H. H., "The Numerical Solution of Parabolic and Elliptic Differential Equations," *Journal of the Society for Industrial and Applied Mathematics*, Vol. 3, No. 1, 1955, pp. 28–41.

[32] Chang, C.-L., and Merkle, C. L., "The Relation between Flux Vector Splitting and Parabolized Schemes," *Journal of Computational Physics*, Vol. 80, No. 2, 1989, pp. 344–361.

[33] Patankar, S. V., *Numerical Heat Transfer and Fluid Flow*, Taylor and Francis, Philadelphia, PA, 1980.

[34] Batten, P., Leschziner, M. A., and Goldberg, U. C., "Average-State Jacobians and Implicit Methods for Compressible Viscous and Turbulent Flows," *Journal of Computational Physics*, Vol. 137, No. 1, 1997, pp. 38–78.

[35] Coakley, T. J., and Huang, P. G., "Turbulence Modeling for High-Speed Flows," AIAA Paper 92-04366, 1992.

[36] Wilcox, D. C., *Turbulence Modeling for CFD*, DCW Industries, La Cañada, CA, 1994.

[37] Riggins, D. W., McClinton, C. R., and Vitt, P. H., "Thrust Losses in Hypersonic Engines. Part I: Methodology," *Journal of Propulsion and Power*, Vol. 13, No. 2, 1997, pp. 281–287.

[38] Mao, M., Riggins, D. W., and McClinton, C. R., "Numerical Simulation of Transverse Fuel Injection," *CFD Symposium in Aeropropulsion*, NASA Lewis Research Center, Cleveland, OH, NASA CP-3078, April 1990.

J. Powers
Associate Editor